Power Balance and Temperature in Optically Pumped Spasers and Nanolasers

Gerold V. Kristanz,[†] Nikita Arnold,*[,†,‡,§] Alexander V. Kildishev,[∥] and Thomas A. Klar[†]

[†]Institute of Applied Physics, Johannes Kepler University, Altenberger Straße 69, 4040, Linz, Austria
[‡]Institute of Semiconductor and Solid State Physics, Johannes Kepler University, Altenberger Straße 69, 4040, Linz, Austria
[∥]Birck Nanotechnology Center, School of ECE, Purdue University, West Lafayette, 1205 West State Street, Indiana 47907-2057, United States

S *Supporting Information*

ABSTRACT: Spasers and nanolasers produce a significant amount of heat, which impedes their realizability. We numerically investigate the farfield emission and thermal load in optically pumped spasers with a coupled electromagnetic/thermal model, including additional temperature discontinuities due to interfacial Kapitza resistance. This approach allows to explore multiple combinations of constitutive materials suitable for robust manufacturable spasers. Three main channels of heat generation are quantified: metal absorption at pumping and spasing wavelengths and nonradiative relaxations in the gain material. Out-radiated power becomes comparable with absorption for spasers of realistic dimensions. Two optimized spaser configurations emitting light near 520 nm are compared in detail: a prolate metal-core/gain-shell and an oblate gain-core/metal-shell. The metal-shell design, which with the increasing size transforms into a metal-clad nanolaser, achieves an internal light-extraction efficiency of 22.4%, and stably operates up to several hundred picoseconds, an order of magnitude longer than the metal-core spaser.

KEYWORDS: plasmonics, spasing, gain saturation, nanoparticle heating, power balance, light extraction efficiency, Kapitza resistance, core−shell spheroids
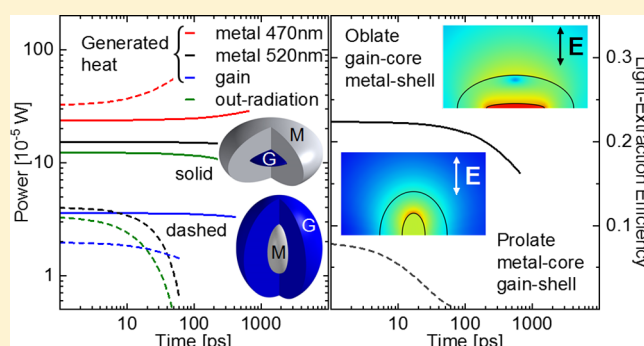
One of the principal problems of the realization of a spaser (surface plasmon amplifier using stimulated emission) and metal-clad nanolaser is that there will be strong fields in an absorbing metal component and its vicinity.[1] As metals are very good at converting electromagnetic energy into heat, this increases the temperature of the system. In general, the heating of plasmonic nanostructures is interesting in two different aspects: either the heating is a desired effect, for example, for electrothermoplasmonic nanotweezers in microfluidic channels[2] or medical applications of nanoparticles in living tissues,[3] or it threatens the realizability of a device. In lowest order approximation, the surface plasmon oscillations in a spaser decay primarily through ohmic loss. The spasing modes also loose energy through far-field radiation (e.g., when used as a nanoscopic light source). In the quasi-static case, this is a weaker effect, but for the spasers of realistic dimensions, especially for "bright" dipolar modes, this channel may become comparable with absorption and important; it is included in our study. In a realistic setting, a temperature change of several hundred degrees in a fraction of a nanosecond is possible. The thermal behavior of spasers and surface plasmons has been discussed by several groups. For example, Smalley et al.[4] derived a framework for the temperature dependence of the

spontaneous emission in semiconductor nanolasers (primarily photonic, but also plasmonic), and estimative approximations regarding the heating of spasers have been carried out by Fedorov et al.[5] However, a comprehensive analysis of the thermal behavior of an operating spaser, as presented in the following study, was missing so far. We aim to provide practical guidelines for experimenters primarily on two subjects, suggest realistic geometries for individual spasers and give estimates for pumping intensities and durations, as well as expected out-radiation and temperatures. This is the first study combining the effects of spatially dependent gain saturation, retardation and radiative losses (i.e., light extraction), heat generation in both metal and gain material, Kapitza resistance, temperature dependences of material properties, and influence of these factors on the temporal evolution of spasing.

ELECTRODYNAMIC DESCRIPTION OF A SPASER

Gain Dielectric Function. We use the gain dielectric function derived in ref 6

$$\varepsilon_G = \varepsilon_h - \varepsilon_L \frac{(\omega_{21} - \omega_s + i\gamma_L/2)(\gamma_L/2)}{(\omega_{21} - \omega_s)^2 + (\gamma_L/2)^2(1 + (|\mathbf{E}_s|/E_{sat})^2)}$$

(1)

which is based on a simplified 4-level scheme for the chromophores (see Figure 1) and accounts for gain saturation

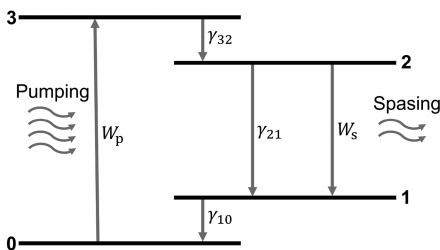**Figure 1.** Simplified 4-level scheme used to model the chromophores. The pumping transition is from levels $0 \rightarrow 3$, and the spasing transition is from levels $2 \rightarrow 1$. We assume fast relaxation from levels 3 and 1, $(\gamma_{32}, \gamma_{10}) \gg (W_s, W_p, \gamma_{21})$.

(SI units are used in this work). The underlying assumptions are fast dephasing of the chromophore polarizations $\gamma_L \gg \gamma_{ij}$ and fast relaxation from levels 3 and 1 $(\gamma_{32}, \gamma_{10}) \gg (W_s, W_p, \gamma_{21})$. Here, ω_s is the frequency of surface plasmon oscillations (the spasing frequency internally established in the system) and ε_h is the dielectric function of the gain host material. The emission of the chromophores is described by a Lorentzian with strength ε_L and width γ_L, centered at a fixed, central free-space wavelength corresponding to the $2 \rightarrow 1$ molecular transition, $\lambda_{21} = 2\pi c/\omega_{21}$, with c being the vacuum speed of light. The dimensionless amplitude of the emission Lorentzian at midline, ε_L, is called (unsaturated) gain level. It is directly related to the pumping rate $W_p[s^{-1}]$ (adapted from eqs 18 and 22 in ref 6),

$$\varepsilon_L = \frac{c}{\omega_s}\sqrt{\varepsilon_h}N_{tot}\sigma_{21}\frac{W_p}{\gamma_{21} + W_p}$$

(2)

where N_{tot} is the density of the chromophores and σ_{21} is their (orientation-averaged) emission cross section in the bulk host medium. The pumping rate W_p depends on the (local) pumping field $\mathbf{E}_p$ and the chromophore bulk absorption cross section (we assume $\sigma_{30} = \sigma_{21}$),

$$W_p = \frac{c\varepsilon_0\sqrt{\varepsilon_h}\sigma_{30}}{2\hbar\omega_p}|\mathbf{E}_p|^2$$

(3)

where the pumping frequency ω_p corresponds to a free-space wavelength of λ_p. We assume that the spaser is tuned close to the $2 \rightarrow 1$ transition of the chromophores, meaning that $\omega_s - \omega_{21} \ll \gamma_L$. The spasing rate W_s can be analogously expressed by replacing $\omega_p \rightarrow \omega_s$, $\mathbf{E}_p \rightarrow \mathbf{E}_s$ and $\sigma_{30} \rightarrow \sigma_{21}$, where $\mathbf{E}_s$ is the local, surface plasmon (spasing) field. Saturation field E_{sat} in eq 1 can be expressed as follows from eq 21 in ref 6

$$E_{sat}^2 = \frac{2\hbar\omega_s(\gamma_{21} + W_p)}{c\varepsilon_0\sqrt{\varepsilon_h}\sigma_{21}}$$

(4)

It can be understood as the strength of the spasing field at which gain saturation effects become significant. For example, at $|\mathbf{E}_s| \approx E_{sat}$ (which corresponds to $W_s \approx W_p + \gamma_{21}$), the gain dielectric function (at midline) is halved with respect to the nonsaturated expression. Finally, γ_{21} is the Purcell-enhanced

spontaneous decay into the resonant mode for the $2 \rightarrow 1$ transition. From quantum-mechanical treatment,[7,8] we estimate (see Supporting Information, end of the section *Purcell-Enhanced Spontaneous Emission*, and Table 2 for values)

$$\gamma_{21} = \frac{c\sigma_{21}}{V_G\sqrt{\varepsilon_h}}$$

(5)

where V_G is the effective mode volume in the gain material.

In calculations we used the following parameters, which are typical for organic fluorophores: $\lambda_{21} = 520$ nm, $\gamma_L = 3.8 \times 10^{14}$ s^{-1}, $N_{tot} = 8 \times 10^{25}$ m^{-3}, $\sigma_{21} = 2.5 \times 10^{-20}$ m^2, and $\lambda_p = 470$ nm, and the gain host is chosen to be silica with $\varepsilon_h = 2.14$.[9]

In detailed analysis of the spaser,[10] (end of section 2.1 there) a chromophores concentration of $N_{tot} = 2.4 \times 10^{26}$ m^{-3} was assumed. Experiments[11] implied $N_{tot} = 4.7 \times 10^{26}$ m^{-3} within a 5 nm thick doped silica shell. In the current study, we use concentrations, that are a factor of 3−5 less and are easier to achieve experimentally.

While mean-field chromophore interaction is included via a field- and position-dependent dielectric function with gain saturation (1), we do not discuss more complex cooperative effects,[12,13] assuming that they are smeared out by strong dephasing and random dipole orientations. Indeed, in the recent paper,[14] Petrosyan and Shahbazyan concluded that with tens of thousands randomly oriented molecules, the ensemble-averaged dipole−dipole coupling vanishes, and the resonant mode is also unaffected by it.

Spasing Threshold. The spasing threshold corresponds to the minimum pumping strength required to start and maintain the generation. For simulations, it is more convenient to express the spasing threshold in terms of the gain level ε_L and not the pumping rate W_p. To find the threshold numerically, we vary the spasing frequency ω_s and the gain level ε_L to find the set of parameters $(\omega_{thr}, \varepsilon_{L,thr})$, for which the electric field diverges in an unsaturated, linear system (i.e., with $(|\mathbf{E}_s|/E_{sat})^2 \rightarrow 0$ in eq 1, see Arnold et al.[15]). ω_{thr} is called the threshold generation frequency of the spaser, while $\varepsilon_{L,thr}$ will be referred to as the gain threshold. After the pair $(\omega_{thr}, \varepsilon_{L,thr})$ is found, all simulations are carried out with gain saturation included.

Heat Sources in Spasers. In an operating spaser, the heat released in the metal can be described by the volumetric power of Ohmic losses, Q, using the imaginary part of the metal dielectric function $\varepsilon_M''(\omega)$,

$$Q(\omega, \mathbf{r}) = \frac{1}{2}\omega\varepsilon_0\varepsilon_M''(\omega)|\mathbf{E}(\omega, \mathbf{r})|^2$$

(6)

where $\mathbf{E}(\omega, \mathbf{r})$ is the amplitude of the electric field at the location $\mathbf{r}$ inside the metal, either at the spasing or the pumping frequency.

The gain material is heated by nonradiative decay of the chromophores. The corresponding heat source can be described by (see Supporting Information, section *Heat Source in the Gain Material*)

$$Q_G = N_{tot}(\hbar\omega_{10} + \hbar\omega_{32})\frac{W_p(W_s + \gamma_{21})}{W_p + W_s + \gamma_{21}}$$

(7)

MULTISCALE AND MULTIPHYSICS NUMERICAL MODELING

Coupling of the Thermal and Electromagnetic Problems. The coupling between the electromagnetic and the thermal problem is achieved via a temperature-dependent

metal dielectric function (see Supporting Information, section *Temperature-Dependent Drude Model*, and Reddy et al.[16]). To simulate the surface plasmon oscillations in a spaser, we use COMSOL Multiphysics, which is a versatile commercial software package based on the finite element method (FEM). We combine nonlinear Maxwell's equations (solved in the frequency domain) with the heat equation (solved in the time domain) using a so-called frequency-transient study step sequence: first, we solve the electromagnetic problem with gain saturation in frequency domain and use its results (i.e., the heat sources) to make a time step in the thermal problem. Then, we recompute all related quantities (e.g., the temperature-dependent dielectric function) and solve the electromagnetic problem again, using the previous solution as an initial guess. The underlying assumption for the validity of this multiscale and multiphysics computational workflow is that the electromagnetic problem approaches equilibrium much faster than the thermal one. In particular, quantum coherence effects[17−20] are omitted in our analysis. Polarization adiabatically tracks the populations for times longer than the dephasing time γ_L^{-1} (inverse atomic line width). Note that recent experiments,[21,22] which reveal pronounced coherence effects in plasmonic systems, essentially deal with single emitters, which makes influence of dephasing much less crucial, as opposed to more than 1000 emitters discussed here. Transients in plasmon and population dynamics end on the time scale of Purcell-enhanced atomic relaxation time γ_{21}^{-1} that is, within dozens of picoseconds at most (Table 2), as vibronic relaxations γ_{32}, γ_{10} and plasmon decay are even faster. Detailed quantum analysis of spaser in ref 23 shows eqs 33−37 and Figures 4 and 5 in Supporting Information there, and the discussion in eq S8 on pp S4 and S5 of Supporting Information, that generation stabilizes below 1 ps (see also Figure 4a,b in ref 10). We study much longer time scales of 10 ps to 1 ns, under constant pumping intensity. Transient ps processes do exist, but the heating during this time is negligible (see Figure 3). Thermal dynamics occurs over larger time scales, where quasi-stationary electrodynamics adiabatically follows slow changes in parameters. Such slowly varying envelope approach fails, if the duration of the transient processes $O(\text{ps})$ becomes comparable with polarization dephasing time $O(\text{fs})$. Fortunately, this is almost never the case.

The electrodynamic simulations of the pumping field are carried out at pumping frequency ω_p, and they must be decoupled from the spasing simulations (which are performed at spasing frequency ω_s). Equation 1 describes the emission properties of chromophores near the spasing frequency, but there is also a Lorentzian with opposite sign around $\omega_{30} = \omega_p$ (i.e., the $3 \rightarrow 0$ transition of the dyes), which corresponds to the absorption cross section. Then, the gain dielectric function for the pumping simulation is[6]

$$\varepsilon_G(\omega_p) = \varepsilon_h + i\frac{c\sqrt{\varepsilon_h} N_{tot} \sigma_{30}/\omega_p}{1 + (|\mathbf{E}_p|/E_{p,sat})^2} \quad (8)$$

where $E_{p,sat}$ is the local pumping saturation field,

$$E_{p,sat}^2 = \frac{2\hbar\omega_p(\gamma_{21} + W_s)}{c\varepsilon_0\sqrt{\varepsilon_h}\sigma_{30}} \quad (9)$$

The heat released in the gain material is already addressed by eq 7 (which is implemented in the spasing simulation); thus, we only have to consider the heat released in the metal.

For computational efficiency, the problem can then be further decoupled: the temperature only needs picoseconds to spread over the metal due to its high thermal diffusivity, but the thermal problem needs several nanoseconds to reach the stationary solution. The high thermal conductivity of the metal further means that the temperature gradient is very small there. Thus, we can assume a homogeneous metal temperature and run many purely electrodynamic pumping simulations for various metal dielectric functions $\varepsilon_M(T)$, where T varies within 300−1200 K. From these results, we can then build a temperature-dependent pumping heat source $Q_p(T)$ (see eq 6). For example, the metal dielectric function at temperature T is $\varepsilon_M(T)$, and the average power of the pumping heat source per unit volume is

$$Q_p(T) = \frac{\omega\varepsilon_0}{2V_M} \int_M dV \varepsilon_M''(T)|\mathbf{E}_p|^2 \quad (10)$$

where V_M is the metal volume and $\mathbf{E}_p$ is the local pumping field induced by an incident (plane wave) intensity I_{in} (which is the same in all simulations). If done thoroughly for an array of temperatures (steps on the order of 1 K), this method improves convergence and is in good agreement with the results from a continuously coupled electromagnetic/thermal numerical model.

Kapitza Resistance. In the thermal simulations, we employ the Kapitza resistance[24,25] in a form of interfacial thermal boundary condition. Due to the Kapitza resistance, which is essential for nanostructures, the temperature is discontinuous at the interface between two materials. The step in temperature is proportional to the heat flux J across the boundary S,

$$J|_S = G(T_1 - T_2) \quad (11)$$

where T_1 and T_2 are the corresponding surface temperatures on either side of the interface. G is called interfacial thermal conductance and depends on the materials and type of interface (e.g., metal/water, metal/metal, ...). The stationary temperature distribution around a continuously heated, spherical nanoparticle provides an estimation of the importance, and good motivation for the inclusion of the Kapitza resistance. The relative change in temperature at the boundary in this case is (see Supporting Information, section *The Stationary Solution for a Continuously Heated, Spherical Nanoparticle with Kapitza Resistance*)

$$\frac{T_1 - T_2}{T_2} = \frac{k_a}{Ga} \quad (12)$$

where a is the nanoparticle radius and k_a is the thermal conductivity of the ambient. Thus, the smaller the nanoparticle, the larger is the influence of the Kapitza resistance.

Geometry, Materials, and Pumping. To explore the operational thermodynamics of example spaser designs, we choose them from a family of coaxial oblate or prolate spheroidal core−shell configurations with a variable core aspect ratio $\kappa > 1$. The pumping field can be parallel or perpendicular to the axis of revolution. The shell spheroid is defined with a shell thickness h: for a core spheroid with a major semiaxis a and a minor semiaxis a/κ, the major and minor semiaxes of the shell will be $a + h$ and $a/\kappa + h$, respectively. Examples for $a = h = 30$ nm, $\kappa = 6.25$ and $a = h = 23$ nm, $\kappa = 1.94$ are shown in Figure 2, panels a, b and c, d, respectively.
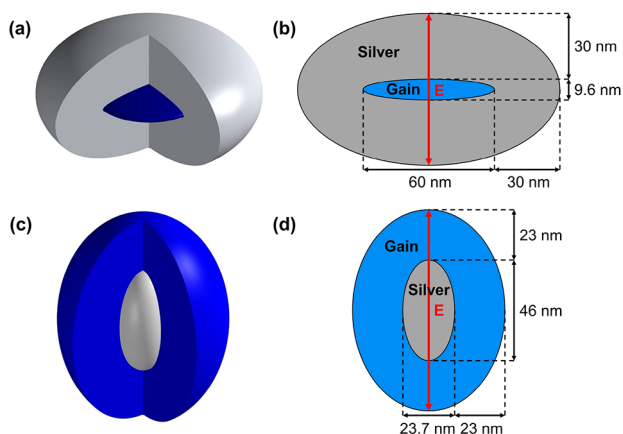
Figure 2. Geometries of the investigated spasers. Both spasers are numerically tuned to a resonant wavelength of 520 nm via variation of their core aspect ratios. The polarization of the pumping field (denoted **E**) is parallel to the axis of revolution. (a) and (b) The oblate gain-core/metal-shell configuration has a core aspect ratio $\kappa = 6.25$. (c, d) Prolate metal-core/gain-shell configuration has a core aspect ratio $\kappa = 1.94$. For both configurations the ambient material is water.

To examine the thermal dynamics of the metal-core/gain-shell and gain-core/metal-shell configuration, it is important to clarify some basic specifications for both structures. We choose silver for metal components (dielectric function by Johnson and Christy[35]) and silica ($\varepsilon_h = 2.14$[9]) as gain host material. Both spasers are immersed in water ($\varepsilon_a = 1.78$[36]) to imitate realistic experimental conditions. Both spasers have similar dimensions, low gain thresholds ($\varepsilon_{L,thr} < 0.15$), and the same generation frequency, which lies in the visible range. Table 1

Table 1. Room Temperature Values of Thermal Material Properties (Thermal Conductivity k, Specific Heat Capacity c, Density ρ) for Silver (Ag), Silica (SiO$_2$), and Water (H$_2$O)

		Ag[26−28]	SiO$_2$[29−31]	H$_2$O[32−34]
k	[W/(m·K)]	426.4	2.40	0.61
c	[J/(kg·K)]	236.7	748	4181.5
ρ	[kg/m^3]	10470	2196	998

shows the room temperature values for the thermal material properties. With the exception of the Kapitza conductance, all material properties are assumed to be temperature-dependent. The values for the Kapitza conductance vary widely in the literature,[37−43] so we choose a temperature-independent Kapitza conductance $G = 10^8$ W/(m^2·K) for all interfaces, which is close to 6×10^7 W/(m^2·K) found in our recent thermoreflectance experiments.[44]

From quasistatic results (see Supporting Information, section *Quasistatic Spasing Condition for Confocal Spheroidal Core-Shell Structures*), we find that three spaser configurations have low gain thresholds ($\varepsilon_{L,thr} < 0.15$) and generation frequencies in the visible range. For the final comparison, we choose to simulate only two essentially different geometries with respect to shape and order of materials: the oblate gain-core/metal-shell structure with **E**∥**z** and the prolate metal-core/gain-shell structure with **E**∥**z**, where **z** represents the axis of revolution. For the excitation field used, both structures show rotational symmetry, which is convenient for simulations. The omitted third oblate spaser with the nonsymmetric

excitation along the large axis also has marginally higher threshold than these two. The spasers are tuned to a generation wavelength of 520 nm via variation of their core aspect ratio. At 520 nm, the gain threshold has a local minimum and the aspect ratios are realistic (i.e., the structures are not unrealistically thin). We set the pumping frequency ω_p to 470 nm, which corresponds to a Stokes difference typical for organic dyes in this spectral range. In ref 10 (middle of the section 1.1 there), a spaser with a (spherical) gain core of radius 12 nm and metal shell thickness below 1 nm are discussed. In the case of manufacturing issues, a simple suggestion to scale the device up by a factor of 2 or 3 could be offered. Our studies reveal that such an easy fix will not work for several reasons: retardation, out-radiation, and thermal effects. To provide the guidelines for the experiments, we kept the wavelength, metal and gain thicknesses and the chromophore concentration as realistic as possible. This unavoidably leads to larger sizes discussed here, which can be also easier to manufacture. The resulting spaser geometries are shown in Figure 2. Such numbers and geometries are feasible for modern methods of dye-matrix manufacturing (for instance, using stimulated emission depletion (STED) lithography[45]). The values of the numeric spasing thresholds are listed in Table 2 among other operational parameters.

Table 2. Operational Parameters for the Gain-Core/Metal-Shell (Gain/Metal) and the Metal-Core/Gain-Shell (Metal/Gain) Spaser in Comparison[a]

		gain/metal	metal/gain
ε_L	[1]	0.193	0.197
$\varepsilon_{L,thr}$	[1]	0.113	0.116
λ_{thr}	[nm]	519.96	519.78
$W_p^\dagger$	[1/s]	1.10×10^{12}	1.02×10^{11}
$W_s^\dagger$	[1/s]	1.08×10^{12}	2.29×10^{10}
γ_{21}	[1/s]	2.83×10^{11}	2.32×10^{10}
I_{in}	[W/cm^2]	2.16×10^7	5.39×10^7

[a]Quantities marked with † depend on position and time: they are averaged over the gain material and evaluated at $t = 0$ (which corresponds to $T = 300$ K).

The pumping strength of a spaser is a key parameter for its operation. It can be expressed in terms of several quantities (which are all related to each other): (i) the pumping rate W_p, (ii) the gain level ε_L, or (iii) the incident pumping intensity I_{in} of a focused pumping laser, which induces the field $\mathbf{E}_p$ in eq 3. We are interested in the case of post-threshold pumping, thus we simulate our spasers at the gain level $\varepsilon_L = 1.7\varepsilon_{L,thr}$. The corresponding parameters (W_p, I_{in}, ...) can be found in Table 2.

Thermal Limits. There are several factors that determine the thermal limitations of a spaser. Generally, a deformation of the geometry should be avoided, which means that the operating temperature should stay below the melting point of the gain host and the metal, respectively. However, Inasawa et al.[46] show that laser-induced surface reshaping of gold nanoparticles occurs approximately 120 degrees below the melting point. The melting point of silver is at 1235 K,[31] which yields an estimated reshaping temperature of around 1115 K. To be on the safe side, we set the maximally allowed metal temperature to 1000 K.

Also critical is the thermal decomposition of the chromophores: if the dye molecules are thermally damaged, the changes of the absorption and emission spectra are

irreversible and the principal functionality of the spaser is threatened. The thermal decomposition temperatures of certain dyes can be quite low, for example, rhodamine B decomposes at around 520−570 K.[47,48] To safely avoid thermal damage of the chromophores, the temperature of the gain material should not exceed 500 K, which makes this a dominant limitation for the combination of materials used here. Since silica has a melting point of 1986 K,[31] this condition also prevents melting effects in the gain host.

■ RESULTS

Figure 3 shows the results for the average and maximum temperatures over time in the respective spaser components.
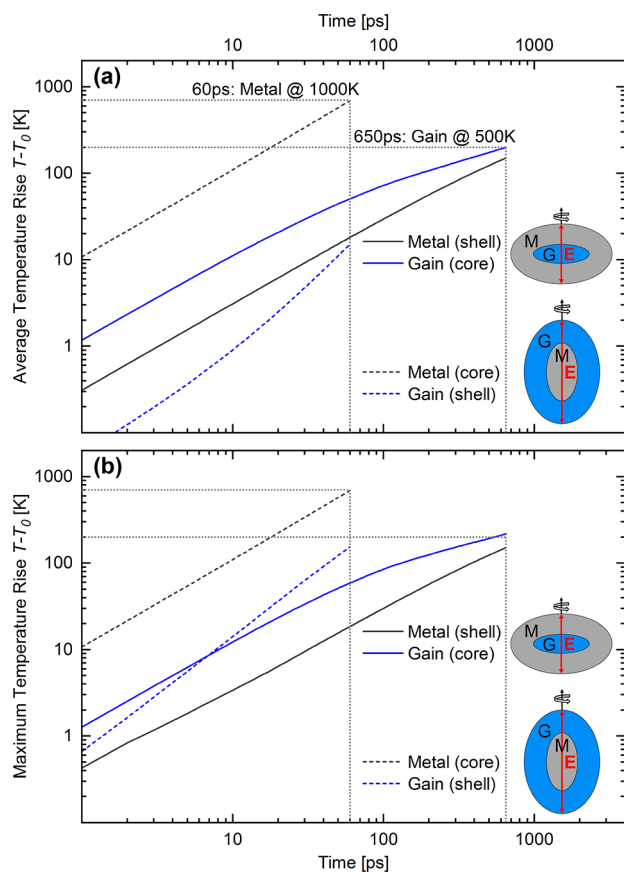

Figure 3. (a) Average and (b) maximum temperature rise $T − T_0$ in the respective spaser components (metal and gain). Solid curves are for the oblate gain-core/metal-shell, dashed curves for the prolate metal-core/gain-shell spaser. The maximum operation time is 650 and 60 ps, respectively (see section Thermal Limits for the thermal limits). Due to the high thermal conductivity of silver, there is practically no difference between average and maximum temperature in the metal.

The oblate gain-core/metal-shell spaser can operate up to 650 ps under the specified pumping conditions before the gain host reaches the critical temperature of 500 K. For the prolate metal-core/gain-shell spaser, the metal component is the limiting factor: after approximately 60 ps, the metal core reaches a temperature of 1000 K and spaser operation needs to be terminated to avoid melting or surface reshaping effects. Thus, the maximum pulsed operation times are 650 and 60 ps, respectively. For information regarding the cooling of the structures on a nanosecond time scale, see Supporting Information, section Cooling Time.

Figure 4 shows the distribution of the spasing field $|\mathbf{E_s}|$ at the end of the pumping pulse (650 or 60 ps) in both
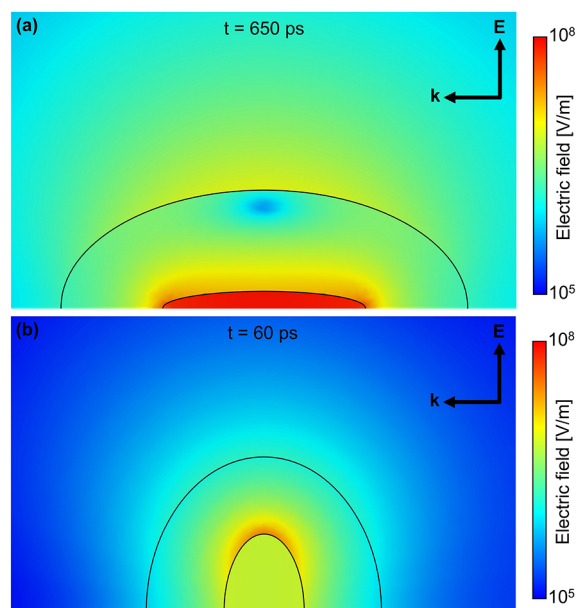

Figure 4. Distribution of the spasing field $|\mathbf{E_s}|$ at the end of the pumping pulse in (a) the oblate gain-core/metal-shell and (b) the prolate metal-core/gain-shell spaser. Wavevector $\mathbf{k}$ refers to the pumping field, while $\mathbf{E}$ indicates the prevalent polarization of both pumping and spasing fields.

configurations. The spasing mode is dipolar in both cases. For the gain-core/metal-shell geometry, the field is approximately an order of magnitude stronger in the core, which leads to more effective chromophore utilization. The field in the oblate gain core is quite homogeneous, and with the increasing size, such a design transforms into a metal-clad nanolaser,[4,49] operating on the first TM mode (dipolar Mie void plasmon in the case of a spherical core−shell). Thus, our analysis bridges the gap between spasers and nanolasers. The small dip in the electric field within the shell of the gain-core/metal-shell oblate spaser is most likely a needle effect: the large curvature along the equator of the "pancake" (left and right sides of the structure in Figure 4a) leads to the disproportionately large fields in this region. The dip is very shallow: the field falls approximately 15%.

Figure 5 shows the temperature distribution at the end of the pumping pulse (650 or 60 ps). Due to the high thermal conductivity of silver, the metal temperature is spatially almost constant in both configurations. In the metal-core/gain-shell spaser, the gain-shell acts as a thermally insulating layer: after 60 ps, the heat wave has penetrated only the first 13 nm of the approximately 23 nm thick gain-shell. In order to diffuse through the shell and reach the ambient, the heat wave would need approximately 175 ps, much longer than the maximally allowed pulse length. For the gain-core geometry, metal is in direct contact with water, which represents the ultimate heat sink. Since most of the heat is generated inside the metal, the operation temperature in this structure is much lower than in its counterpart. Because of the Kapitza resistance, the temperature jumps at the metal-gain interface: in Figure 5, the discontinuity is 40 K for the gain-core/metal-shell and 540 K for the metal-core/gain-shell spaser. The average curvature
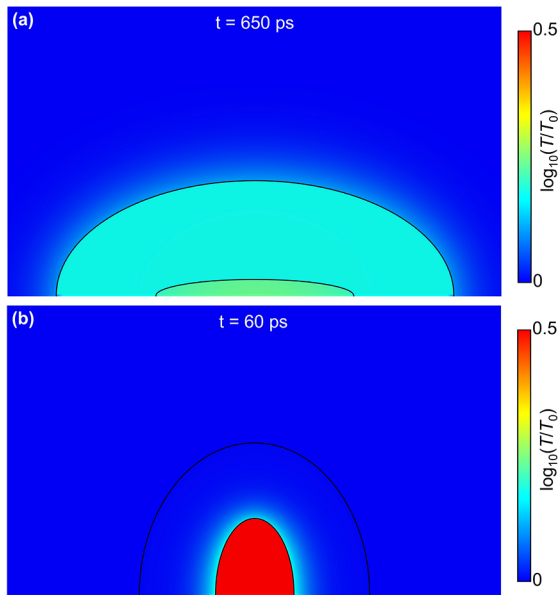
Figure 5. Temperature distribution at the end of the pumping pulse in (a) the oblate gain-core/metal-shell and (b) the prolate metal-core/gain-shell spaser. For the latter, the shell acts as a thermally insulating layer. Note that the scale is logarithmic from $T_0 = 300$ K to $T \approx 950$ K.
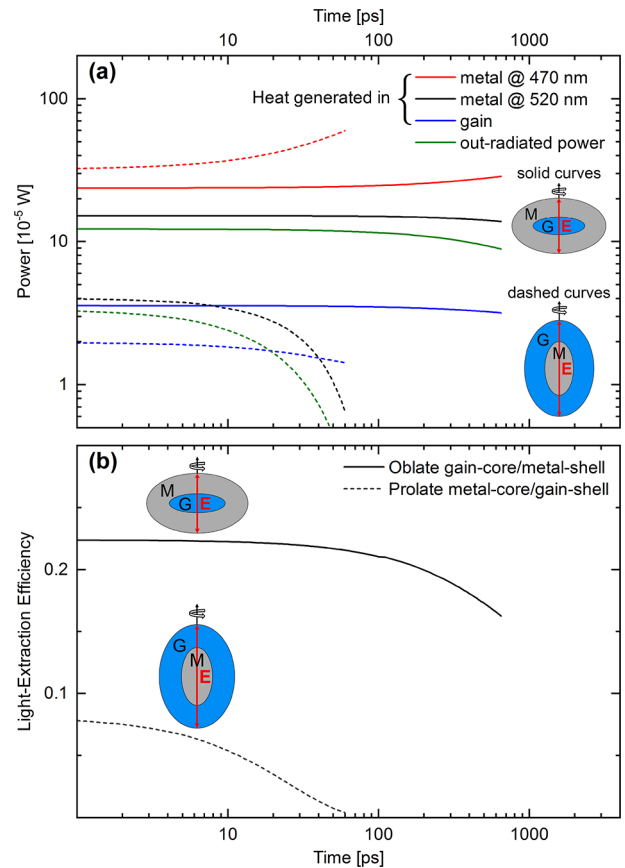

Figure 6. (a) Heating power (integrated heat sources) in the respective spaser components and the out-radiated power (integrated far-field Poynting vector of the spasing field) for both spasers: oblate gain-core/metal-shell (solid curves) and prolate metal-core/gain-shell (dashed curves). The maximum operation times are 60 and 650 ps. The heat generated at the spasing/pumping frequency in the metal is induced by the spasing/pumping field ($\mathbf{E}_s$, $\mathbf{E}_p$), respectively. (b) Internal light-extraction efficiency of both spasers, calculated as described in the text.

of the prolate spaser is larger and its temperature is higher, hence, the temperature discontinuity is more pronounced.

We apply the thermal restrictions of section Thermal Limits to the average rather than the maximum temperature. For the metal component, the choice is irrelevant: the temperature difference over the volume is of the order of 1 K, and the average and maximum temperatures largely coincide (black curves in Figure 3). In the gain material, however, intense temperatures can occur at the gain/metal interface (especially if the gain shell acts as an insulating layer). The affected area is very small though (only the first few nm, see Figure 5b), so slight melting effects or chromophore decomposition are almost negligible. In fact, thermal destruction of chromophores in close proximity to the metal might even be beneficial: Kewes et al.[23] argue that a nonactive layer of a few nanometers around a metal core reduces quenching (i.e., the excitation of undesired, higher-order surface plasmon modes). In real systems, the heat generated by the Ohmic decay of higher-order surface plasmons may be significant, thus, a nonactive "spacing" layer can prove thermally advantageous.

The contributions of different heat souces to the total heating power in the spasers are shown in Figure 6a. For the gain-core/metal-shell spaser (solid curves), the heat induced by the spasing (at 520 nm) and pumping (at 470 nm) fields is comparable, while for the metal-core/gain-shell spaser (dashed curves), the pumping field heat source is the dominating contribution. In both cases, the heat generated by vibronic relaxation of the chromophore excitation is negligible compared to the total heating power. Though metal absorption at pumping wavelength is the largest heat source, the results show that pulsed operation of both devices is feasible.

The opposite temporal behavior of the spasing and pumping heating powers in Figure 6a is due to an increase in temperature with time. To understand both trends, we have to look at the temperature dependence of the Ohmic loss, eq 6: $Q(T) \propto \varepsilon_M''(T)|\mathbf{E}(T)|^2$. The imaginary part of the metal

dieletric function increases linearly with temperature, $\varepsilon_M'' \propto C_1 + C_2 T$, while ε_M' remains effectively constant (see Supporting Information, section Temperature-Dependent Drude Model). The pumping field, which is off-resonant, is largely dominated by the absolute value of the dielectric function, which in turn remains approximately constant since $|\varepsilon_M'| \gg |\varepsilon_M''| \Rightarrow |\varepsilon_M| \approx |\varepsilon_M'| \approx \mathrm{const}(T)$. Thus, the pumping field $\mathbf{E}_p$ depends only weakly on temperature and the pumping heat source Q_p increases linearly with temperature, since

$$Q_p(T) \propto \varepsilon_M''(T) \tag{13}$$

The temperature dependence of the spasing field in the metal can be qualitatively understood using the quasistatic estimation for the gain-core/metal-shell spaser at the threshold generation frequency ω_{thr} (see eq S32 in Supporting Information, section Quasistatic Estimation for the Temperature Dependence of the Spasing Field at the Threshold Generation Frequency, and the discussion there),

$$|\mathbf{E}_s(\omega_{thr}, T)|^2 \propto E_{sat}^2 \left(\frac{\varepsilon_L |\varepsilon_M'|}{\varepsilon_h \varepsilon_M''(T)} - 1 \right) \tag{14}$$

The saturation field E_{sat} and the gain level ε_L are related to the pumping field $\mathbf{E}_p$, see eqs 2–4, and depend only weakly on

temperature. Thus, the spasing heat source Q_s decreases almost linearly with temperature,

$$Q_s(T) \propto \frac{\varepsilon_L |\varepsilon'_M|}{\varepsilon_h} - \varepsilon''_M(T) \qquad (15)$$

Additionally, in Figure 6a, the farfield out-radiated power (green curves) is shown. For both geometries, it is comparable with the absorption of the spasing field by the metal (black curves). This contrasts with the often used quasistatic assumption, that the dominant losses of the generating spaser are purely absorptive.[10] Such an approximation indeed holds for a spaser of few nm in size, but for a realistic geometry with sizes around 100 nm studied here, the retardation effects and radiative losses cannot be neglected. Here, the radiative losses equal about 80% of the absorption losses, which is in qualitative agreement with the numerical gain thresholds for our spasers, which are about 60−70% higher than the quasistatic predictions (see Supporting Information, section *Quasistatic Spasing Condition for Confocal Spheroidal Core−Shell Structures*). The relation between the absorption and out-radiation holds both near and above threshold, when gain saturation sets in, because both are proportional to the square of the spasing field. In an idealized laser with negligible absorptive losses, post-threshold pumping is fully converted into useful output (not counting the Stokes shift). In a spaser, the field in the metal represents an immanent part of the resonant mode, and the out-radiation and Ohmic losses maintain a constant ratio even above threshold.

Importantly, the results in Figure 6a allow for the estimation of the farfield emission efficiency for both spasers. Within the employed approximations, the overall incoming absorbed power is converted into the losses in the metal at the pumping and spasing wavelengths, the losses in the gain material, and the out-radiated power, that is, equals the sum of all four curves in Figure 6a (quenching and scattering at the pumping wavelength are neglected here). Dividing the radiated power (green curves) by this sum, we arrive at an internal farfield light-extraction efficiency, which is shown in Figure 6b. At early times, when the temperature is low, it reaches 22.4% and 8.1% for the oblate and prolate geometries, respectively. While for the prolate geometry, the efficiency degrades to half of the initial value already after only about 16 ps, for the oblate case with the gain core, it remains almost constant, and is still equal to 16.3% at the thermally defined time limit of of 650 ps. This is not overly surprising, as with increasing size this structure becomes similar to a metal-clad nanolaser.[4,49]

The decrease in the radiated power is concomitant with the overall decrease of the spasing field with temperature, and therefore time (see eq 14). For the dipolar modes used here and the numbers considered, the oblate geometry with gain core turns out to be a better farfield emitter of light than the prolate one, both in absolute numbers and in terms of extraction efficiency. This is related to the overall better performance and larger spasing fields there (see Figure 4) and, possibly, to the nature of the metal shell plasmon in this case (low-energy, symmetric, bonding), where surface charges on the outer and inner surfaces of the shell oscillate in phase.[50] Larger out-radiated power (losses) is a desired outcome if a spaser is used as a nanoscopic light source. For the applications where it is employed as a local coherent field amplifier, for instance, for surface-enhanced Raman scattering (SERS), larger local fields are of higher relevance, despite associated

absorption in the metal. Here, prolate geometry, or higher order modes with smaller radiative losses may be preferable.

We also simulated similar spasers with polystyrene as gain host material, which was recently used as a matrix for organic dyes in microresonators.[51−53] The summary of these results can be found in the Supporting Information, section *Polystyrene as Gain Host Material*.

CONCLUSIONS

We have shown that pulsed operation of spasers with durations longer than 10 ps is principally possible with regard to thermal stability. In particular, the considered core−shell configurations with resonances near 520 nm can be operated with pulse lengths up to 60 ps (prolate metal-core/gain-shell) and 650 ps (oblate gain-core/metal-shell) in an aqueous ambient. The latter geometry, which with increasing size becomes similar to a metal-clad nanolaser, provides better utilization of gain material, and the metal/water interface proves to be very efficient in transporting heat to the water ambient, which acts as a heat sink. Further, the optically pumped oblate gain core/metal shell spaser, operated as a nanoscopic coherently radiating light source, reaches an internal light-extraction efficiency of 22.4%, which stays almost constant up until the thermal time limit of 650 ps.

ASSOCIATED CONTENT

Ⓢ Supporting Information

The Supporting Information is available free of charge on the ACS Publications website at DOI: 10.1021/acsphotonics.8b00705.

> Detailed discussions and derivations on several theoretical and numerical aspects, as mentioned throughout the text (PDF).

AUTHOR INFORMATION

Corresponding Author
*E-mail: nikita.arnold@jku.at.

ORCID
Nikita Arnold: 0000-0003-3673-1772
Thomas A. Klar: 0000-0002-1339-5844

Present Address
§Institute of Experimental Physics/Soft Matter Physics, Johannes Kepler University, Altenberger Straße 69, 4040, Linz, Austria.

Notes
The authors declare no competing financial interest.

REFERENCES

(1) Bergman, D. J.; Stockman, M. I. Surface Plasmon Amplification by Stimulated Emission of Radiation: Quantum Generation of Coherent Surface Plasmons in Nanosystems. *Phys. Rev. Lett.* **2003**, *90*, 027402.

(2) Ndukaife, J. C.; Kildishev, A. V.; Nnanna, A. G. A.; Shalaev, V. M.; Wereley, S. T.; Boltasseva, A. Long-range and rapid transport of individual nano-objects by a hybrid electrothermoplasmonic nano-tweezer. *Nat. Nanotechnol.* **2016**, *11*, 53.

(3) Pissuwan, D.; Valenzuela, S. M.; Cortie, M. B. Therapeutic possibilities of plasmonically heated gold nanoparticles. *Trends Biotechnol.* **2006**, *24*, 62−67.

(4) Smalley, J. S. T.; Gu, Q.; Fainman, Y. Temperature Dependence of the Spontaneous Emission Factor in Subwavelength Semiconductor Lasers. *IEEE J. Quantum Electron.* **2014**, *50*, 175−185.

(5) Fedorov, I. A.; Parfenyev, V. M.; Vergeles, S. S.; Tartakovsky, G. T.; Sarychev, A. K. Allowable Number of Plasmons in Nanoparticle. *JETP Lett.* **2014**, *100*, 530−534.

(6) Arnold, N.; Piglmayer, K.; Kildishev, A. V.; Klar, T. A. Spasers with retardation and gain saturation: electrodynamic description of fields and optical cross-sections. *Opt. Mater. Express* **2015**, *5*, 2546−2577.

(7) Yariv, A. *Quantum Electronics*, 3rd ed.; John Wiley & Sons, New York, 1989.

(8) Khurgin, J. B.; Sun, G. Comparative analysis of spasers, vertical-cavity surface-emitting lasers and surface-plasmon-emitting diodes. *Nat. Photonics* **2014**, *8*, 468−473.

(9) Malitson, I. H. Interspecimen Comparison of the Refractive Index of Fused Silica. *J. Opt. Soc. Am.* **1965**, *55*, 1205−1209.

(10) Stockman, M. I. The spaser as a nanoscale quantum generator and ultrafast amplifier. *J. Opt.* **2010**, *12*, 024004.

(11) Noginov, M. A.; Zhu, G.; Belgrave, A. M.; Bakker, R.; Shalaev, V. M.; Narimanov, E. E.; Stout, S.; Herz, E.; Suteewong, T.; Wiesner, U. Demonstration of a spaser-based nanolaser. *Nature* **2009**, *460*, 1110−1112.

(12) Bordo, V. G. Cooperative effects in spherical spasers: Ab initio analytical model. *Phys. Rev. B: Condens. Matter Mater. Phys.* **2017**, *95*, 235412.

(13) Shesterikov, A. V.; Gubin, M. Y.; Karpov, S. N.; Prokhorov, A. V. On the Effect of Dipole-Dipole Interactions on the Quantum Statistics of Surface Plasmons in Multiparticle Spaser Systems. *JETP Lett.* **2018**, *107*, 435−439.

(14) Petrosyan, L. S.; Shahbazyan, T. V. Spaser quenching by off-resonant plasmon modes. *Phys. Rev. B: Condens. Matter Mater. Phys.* **2017**, *96*, 075423.

(15) Arnold, N.; Hrelescu, C.; Klar, T. A. Minimal spaser threshold within electrodynamic framework: Shape, size and modes. *Ann. Phys.* **2016**, *528*, 295−306.

(16) Reddy, H.; Guler, U.; Chaudhuri, K.; Dutta, A.; Kildishev, A. V.; Shalaev, V. M.; Boltasseva, A. Temperature-Dependent Optical Properties of Single Crystalline and Polycrystalline Silver Thin Films. *ACS Photonics* **2017**, *4*, 1083−1091.

(17) Kumarapperuma, L.; Premaratne, M.; Jha, P. K.; Stockman, M. I.; Agrawal, G. P. Complete characterization of the spasing (L-L) curve of a three-level quantum coherence enhanced spaser for design optimization. *Appl. Phys. Lett.* **2018**, *112*, 201108.

(18) Jha, P. K.; Wang, Y.; Ren, X. X.; Zhang, X. Quantum-coherence-enhanced transient surface plasmon lasing. *J. Opt.* **2017**, *19*, 054002.

(19) Gegg, M.; Richter, M. Efficient and exact numerical approach for many multi-level systems in open system CQED. *New J. Phys.* **2016**, *18*, 043037.

(20) Voronine, D. V.; Huo, W. G.; Scully, M. Ultrafast dynamics of surface plasmon nanolasers with quantum coherence and external plasmonic feedback. *J. Opt.* **2014**, *16*, 114013.

(21) Gross, H.; Hamm, J. M.; Tufarelli, T.; Hess, O.; Hecht, B. Near-field strong coupling of single quantum dots. *Science Advances* **2018**, *4*, eaar4906.

(22) Kongsuwan, N.; Demetriadou, A.; Chikkaraddy, R.; Benz, F.; Turek, V. A.; Keyser, U. F.; Baumberg, J. J.; Hess, O. Suppressed Quenching and Strong-Coupling of Purcell-Enhanced Single-Molecule Emission in Plasmonic Nanocavities. *ACS Photonics* **2018**, *5*, 186−191.

(23) Kewes, G.; Herrmann, K.; Rodríguez-Oliveros, R.; Kuhlicke, A.; Benson, O.; Busch, K. Limitations of Particle-Based Spasers. *Phys. Rev. Lett.* **2017**, *118*, 237402.

(24) Kapitza, P. L. Heat Transfer and Superfluidity of Helium II. *Phys. Rev.* **1941**, *60*, 354−355.

(25) Swartz, E. T.; Pohl, R. O. Thermal boundary resistance. *Rev. Mod. Phys.* **1989**, *61*, 605−668.

(26) Suh, I. K.; Ohta, H.; Waseda, Y. High-temperature thermal expansion of six metallic elements measured by dilatation method and X-ray diffraction. *J. Mater. Sci.* **1988**, *23*, 757−760.

(27) Kelley, K. K. *High-Temperature Heat-Content, Heat-Capacity, and Entropy Data for the Elements and Inorganic Compounds*, 1st ed.; U.S. Government Printing Office: WA, 1960.

(28) Powell, R. W.; Ho, C. Y.; Liley, P. E. Thermal Conductivity of Selected Materials. *Technical Report*, 1966.

(29) Lord, R. C.; Morrow, J. C. Calculation of the Heat Capacity of α Quartz and Vitreous Silica from Spectroscopic Data. *J. Chem. Phys.* **1957**, *26*, 230−232.

(30) Jund, P.; Jullien, R. Molecular-dynamics calculation of the thermal conductivity of vitreous silica. *Phys. Rev. B: Condens. Matter Mater. Phys.* **1999**, *59*, 13707−13711.

(31) Haynes, W. M.; Lide, D. R.; Bruno, T. J. *CRC Handbook of Chemistry and Physics*, 97th ed.; CRC Press: Boca Raton, FL, 2017.

(32) Vargaftik, N. B. *Handbook of Physical Properties of Liquids and Gases. Pure Substances and Mixtures*, 2nd ed.; Springer, Berlin, 1975.

(33) Zábranskỳ, M.; Ružička, V., Jr; Domalski, E. S. Heat Capacity of Liquids: Critical Review and Recommended Values. Supplement I. *J. Phys. Chem. Ref. Data* **2001**, *30*, 1199−1689.

(34) de Castro, C. A. N.; Li, S. F. Y.; Nagashima, A.; Trengove, R. D.; Wakeham, W. A. Standard Reference Data for the Thermal Conductivity of Liquids. *J. Phys. Chem. Ref. Data* **1986**, *15*, 1073−1086.

(35) Johnson, P. B.; Christy, R. W. Optical Constants of the Noble Metals. *Phys. Rev. B* **1972**, *6*, 4370−4379.

(36) Hale, G. M.; Querry, M. R. Optical Constants of Water in the 200-nm to 200-μm Wavelength Region. *Appl. Opt.* **1973**, *12*, 555−563.

(37) Barrat, J. L.; Chiaruttini, F. Kapitza resistance at the liquid-solid interface. *Mol. Phys.* **2003**, *101*, 1605−1610.

(38) Ge, Z.; Cahill, D. G.; Braun, P. V. AuPd Metal Nanoparticles as Probes of Nanoscale Thermal Transport in Aqueous Solution. *J. Phys. Chem. B* **2004**, *108*, 18870−18875.

(39) Ge, Z. Nanoscale Thermal Transport at Solid−Liquid Interfaces. *Ph.D. Thesis*, University of Illinois at Urbana-Champaign, 2006.

(40) Shenogina, N.; Godawat, R.; Keblinski, P.; Garde, S. How Wetting and Adhesion Affect Thermal Conductance of a Range of Hydrophobic to Hydrophilic Aqueous Interfaces. *Phys. Rev. Lett.* **2009**, *102*, 156101.

(41) Merabia, S.; Shenogin, S.; Joly, L.; Keblinski, P.; Barrat, J. L. Heat transfer from nanoparticles: A corresponding state analysis. *Proc. Natl. Acad. Sci. U. S. A.* **2009**, *106*, 15113−15118.

(42) Vo, T. Q.; Kim, B. H. Interface Thermal Resistance between Liquid Water and Various Metallic Surfaces. *International Journal of Precision Engineering and Manufacturing* **2015**, *16*, 1341−1346.

(43) Ju, S.; Palpant, B.; Chalopin, Y. Adverse Effects of Polymer Coating on Heat Transport at the Solid-Liquid Interface. *J. Phys. Chem. C* **2017**, *121*, 13474−13480.

(44) Wang, D.; Maize, K.; Song, M.; Boltasseva, A.; Shalaev, V. M.; Shakouri, A.; Kildishev, A. V. Thermoreflectance Imaging of Optically Pumped Gap Plasmon Structures. *Proceedings of the Conference on Lasers and Electro-Optics*, San Jose, CA, May 13−18, 2018; OSA Publishing, 2018.

(45) Wiesbauer, M.; Wollhofen, R.; Vasic, B.; Schilcher, K.; Jacak, J.; Klar, T. A. Nano-Anchors with Single Protein Capacity Produced with STED Lithography. *Nano Lett.* **2013**, *13*, 5672−5678.

(46) Inasawa, S.; Sugiyama, M.; Yamaguchi, Y. Laser-Induced Shape Transformation of Gold Nanoparticles below the Melting Point: The Effect of Surface Melting. *J. Phys. Chem. B* **2005**, *109*, 3104−3111.

(47) Fujii, T.; Ishii, A.; Anpo, M. Absorption and fluorescence spectra of rhodamine B molecules encapsulated in silica gel networks and their thermal stability. *J. Photochem. Photobiol., A* **1990**, *54*, 231−237.

(48) Rhodamine B (C.I. 45170) for microscopy. *Safety Data Sheet*; Carl Roth GmbH und Co. KG, 2016.

(49) Gu, Q.; Smalley, J. S. T.; Shane, J.; Bondarenko, O.; Fainman, Y. Temperature effects in metal-clad semiconductor nanolasers. *Nanophotonics* **2015**, *4*, 26−43.

(50) Prodan, E.; Radloff, C.; Halas, N. J.; Nordlander, P. A Hybridization Model for the Plasmon Response of Complex Nanostructures. *Science* **2003**, *302*, 419−422.

(51) Wei, C.; Liu, S. Y.; Zou, C. L.; Liu, Y.; Yao, J.; Zhao, Y. S. Controlled Self-Assembly of Organic Composite Microdisks for Efficient Output Coupling of Whispering-Gallery-Mode Lasers. *J. Am. Chem. Soc.* **2015**, *137*, 62−65.

(52) Ta, V. D.; Chen, R.; Sun, H. D. Tuning Whispering Gallery Mode Lasing from Self-Assembled Polymer Droplets. *Sci. Rep.* **2013**, *3*, 1362.

(53) Okada, D.; Nakamura, T.; Braam, D.; Dao, T. D.; Ishii, S.; Nagao, T.; Lorke, A.; Nabeshima, T.; Yamamoto, Y. Color-Tunable Resonant Photoluminescence and Cavity-Mediated Multistep Energy Transfer Cascade. *ACS Nano* **2016**, *10*, 7058−7063.

Supporting information for:

Power balance and temperature in optically pumped spasers and nanolasers: supplementary materials

Gerold V. Kristanz,[†] Nikita Arnold,[∗,†,‡,¶] Alexander V. Kildishev,[§] and

Thomas A. Klar[†]

[†]Institute of Applied Physics, Johannes Kepler University, Altenberger Straße 69, 4040, Linz, Austria

[‡]Institute of Semiconductor and Solid State Physics, Johannes Kepler University, Altenberger Straße 69, 4040, Linz, Austria

[¶]Currently at: Institute of Experimental Physics/Soft Matter Physics, Johannes Kepler University, Altenberger Straße 69, 4040, Linz, Austria

[§]Birck Nanotechnology Center, School of ECE, Purdue University, West Lafayette, 1205 W State Street, IN 47907-2057, USA

E-mail: nikita.arnold@jku.at

Number of pages: 19

Number of figures: 2

Number of tables: 2

Purcell-enhanced spontaneous emission

The total spontaneous emission rate of the chromophores from levels 2 to 1 (γ_{21}) includes several channels. The electronic excitation in the dye system can either decay into a resonant (in the present case dipolar) surface plasmon, or it can decay into higher order (non-resonant, multipolar) surface plasmons. It can also decay radiatively (into far-field photons) or non-radiatively (into phonons). Spontaneous emission contributes to noise in a spaser,[S1,S2] which we are not able to simulate within the current frequency-domain framework. Thus, we assume that our systems are "good" single-mode spasers, where the spontaneous emission primarily yields dipolar surface plasmons.

The spontaneous emission rate is Purcell-enhanced,[S3] since the nanoparticle acts as a resonator with a very small mode volume. Quantum-mechanics predicts that the stimulated emission into a given single mode is always a factor n_s stronger than the spontaneous emission into it (see Section 8.3 in Yariv,[S4] Supplement 2 in Khurgin et al.[S2] and Supplement Section 2 in Kewes et al.[S5]), where n_s is the number of resonant surface plasmons:

$$\gamma_{21} = \frac{W_s}{n_s}. \tag{S1}$$

n_s can be expressed in terms of the total electromagnetic (spasing) energy in the system (see §80 in Landau and Lifshitz[S6]),

$$n_s \hbar \omega_s = \frac{1}{4} \int dV \left(\varepsilon_0 \frac{\partial(\omega \varepsilon')}{\partial \omega} |\mathbf{E}_s|^2 + \mu_0 |\mathbf{H}_s|^2 \right). \tag{S2}$$

To get an estimate for γ_{21} used in the rate equations results in the main text, it is convenient to average the number of transitions per unit volume over the gain material,

$$\tilde{\gamma}_{21} n_2 = \int_G dV \gamma_{21} N_2 \qquad \text{with} \qquad n_2 = \int_G dV N_2, \tag{S3}$$

where N_2 is the population density and n_2 the total population of level 2. Inserting the equation for the spasing rate W_{s}, similar to Eq. (3) in the main text,

$$W_{\mathrm{s}} = \frac{c\varepsilon_0\sqrt{\varepsilon_{\mathrm{h}}}\sigma_{21}}{2\hbar\omega_{\mathrm{s}}}|\mathbf{E}_{\mathrm{s}}|^2, \tag{S4}$$

yields (assuming spasing in the center of the line with $\omega_{\mathrm{s}} = \omega_{21}$)

$$\tilde{\gamma}_{21} = \frac{\sigma_{21}c}{\sqrt{\varepsilon_{\mathrm{h}}}}\left(\frac{\frac{1}{2}\int_{\mathrm{G}}dV\,\varepsilon_0\varepsilon_{\mathrm{h}}|\mathbf{E}_{\mathrm{s}}|^2 N_2}{n_{\mathrm{s}}\hbar\omega_{\mathrm{s}}n_2}\right). \tag{S5}$$

The ratio in parentheses quantifies the overlap between the density profiles of the electromagnetic energy w and the population inversion N_2. The result has the dimension of inverse volume:

$$\frac{\frac{2}{4}\int_{\mathrm{G}}dV\,\varepsilon_0\varepsilon_{\mathrm{h}}|\mathbf{E}_{\mathrm{s}}|^2 N_2}{n_{\mathrm{s}}\hbar\omega_{\mathrm{s}}n_2} = \frac{2\int_{\mathrm{G}}dV\,wN_2}{\int_{\mathrm{all}}dV\,w\quad\int_{\mathrm{G}}dV\,N_2} \approx \frac{2W_{\mathrm{G}}N_2}{WV_{\mathrm{G}}N_2} = \frac{2f}{V_{\mathrm{G}}}. \tag{S6}$$

The dimensionless factor $f = W_{\mathrm{G}}/W$ is the fraction of electromagnetic energy stored in the gain material (neglecting small magnetic contributions) vs. total electromagnetic energy in the system, while V_{G} is the modal volume in the gain material, modified by the distribution of population inversion. We assume that half of the energy is located in the gain material, $2f = 1$, approximate V_{G} by the gain volume, (which, for our geometries, is related to the volume of the nanoparticle), and use the averaged value $\gamma_{21} = \tilde{\gamma}_{21}$ everywhere. This leads to our final approximation for the spontaneous emission rate:

$$\gamma_{21} = \frac{\sigma_{21}c}{V_{\mathrm{G}}\sqrt{\varepsilon_{\mathrm{h}}}} = \gamma_{21,\mathrm{bulk}}\frac{\omega}{\gamma_{\mathrm{L}}}\frac{\lambda^3}{(2\pi)^2 n_{\mathrm{h}}^3 V_{\mathrm{G}}}. \tag{S7}$$

The last equality in Eq. (S7) was obtained expressing σ_{21} via the bulk (unmodified) radiative decay rate in the host medium, $\gamma_{21,\mathrm{bulk}}$ (refractive index $n_{\mathrm{h}} = \sqrt{\varepsilon_{\mathrm{h}}}$), (see Eq. (20) in Arnold et al.[S7] and references therein). It contains the quality factor of the atomic line $Q_{\mathrm{L}} = \omega/\gamma_{\mathrm{L}}$,

rather than that of the resonator $Q_{\rm R} = \omega/\gamma_{\rm R}$, which enters the conventional Purcell factor (Eq. (13.3-47) in Saleh and Teich[S8]). The latter is derived for a narrow atomic line $\gamma_{\rm L} \ll \gamma_{\rm R}$, while for organic dyes (or semiconductors) the situation is reversed, or the linewidths are comparable. In such situations, the emission linewidth becomes the dominant factor, see Eq. (37) in Khurgin,[S9] or Eq. (40) in the Supplementary Materials to Khurgin and Sun,[S2] which explicitly discusses this issue.

The first expression in Eq. (S7), (Eq. (5) in the Main Text) elucidates the corpuscular origin of the Purcell enhancement as an increase in collision frequency between the emitter/absorber and the photon, which "moves" with the velocity $c/\sqrt{\varepsilon_{\rm h}}$ within the small modal volume. More detailed expressions for the Purcell factor depend on position (Supplementary Materials to Khurgin and Sun[S2]), include orientational and spatial averaging (Figs. 2ab in Kewes et al.[S5]) and even time dependence, due changes in the field distribution with temperature. To incorporate all this into the model, going beyond the mesoscopic description, would be an overshot in accuracy, diluting the main message of the work, which lies in the analysis of retardation, light extraction and thermal effects, keeping the key parameters within the physically admissible range.

Similarly, quantum coherence effects are smeared out by *both* strong dephasing of the chromophores, *and* the fast decay of plasmons. This can be illustrated as follows. The quantum dynamics of a spaser can be described by three equations: see (4)-(6) in ref.,[S1] or (64)-(67) in ref.,[S10] or (34) in ref.[S11] (the latter discusses also more elaborate models):

$$
\begin{aligned}
\dot{\rho} &= -\left(i(\omega - \omega_{21}) + \Gamma_{21}\right)\rho + ian\Omega^* \\
\dot{n} &= -\gamma_{21}(1 + n) + g(1 - n) - 4\mathrm{Im}(a\rho\Omega) \\
\dot{a} &= (i(\omega - \omega_{\rm M}) - \gamma_{\rm M})a + ia\rho^*\Omega n_{\rm tot}.
\end{aligned}
\tag{S8}
$$

Here, ρ and n are complex amplitudes of non-diagonal and diagonal elements of the density matrix, which describe polarization and population inversion; a is the complex amplitude of

(quasi-classical) plasmon number operator; ω, ω_{21} and ω_M are the frequencies of operation, atomic transition and plasmon, respectively. $\Gamma_{21} = \gamma_L/2$ is the decay of non-diagonal part of density matrix, (i.e., dephasing rate of chromophores, decay of macroscopic polarization), γ_{21} is the depopulation rate of the upper level, including non-radiative and (Purcell-enhanced) radiative contributions, and γ_M is the plasmon decay rate. g is the pumping rate parameter, Ω is the (normalized) Rabi frequency of the spasing transition, and n_{tot} the total number of (identical) chromophores.

These equations contain quantum coherence effects. For example, if the spasing field a is enforced externally (and pumping g is correspondingly removed), all frequencies are equal and damping and dephasing are absent, the last terms in the first two equations in (S8) are oscillatory, with the Rabi frequency $2|a\Omega|$.

All three rates in equations (S8): the dephasing Γ_{21}, Purcell-enhanced relaxation γ_{21} and plasmon decay γ_M, damp any oscillatory processes. These rates are in the range 3×10^{11} to $2 \times 10^{14}\,\mathrm{s}^{-1}$. Thus, any quantum coherence oscillations will be suppressed *at least* within few picoseconds, which is well below the timescales of interest for practical spaser operation.

For such long times, calculations based on quantum density matrix (optical Bloch) equations for the spaser (section 2.1 in ref.[S1]), which do include (strongly damped) coherent effects, result in the (quasi-static) threshold expression (Eq. (82) in similar ref.[S10]), which is *iden-tical* to the one derived from the purely electrodynamic considerations (using appropriate microscopic expression for ε''_{gain}), as noted in ref.[S12] (end of section 3 there). Post-threshold behavior in long pulses is also the same, as discussed in ref.[S7]

Heat source in the gain material

The gain material is heated by non-radiative relaxation and decay of electronic states into various vibronic excitations of the dye chromophores. The corresponding heat source follows

from the corresponding terms in an idealized 4-level system:

$$Q_\mathrm{G} = \hbar\omega_{20}\gamma_{20,\mathrm{nr}}N_2 + (\hbar\omega_{30}\gamma_{30,\mathrm{nr}} + \hbar\omega_{32}\gamma_{32})N_3 + \hbar\omega_{10}\gamma_{10}N_1. \tag{S9}$$

Here, we additionally included non-radiative relaxations from levels $3 \to 0$ and $2 \to 0$ (which are not shown in Fig. 1). The term with $\hbar\omega_{20}$ is more appropriate for non-radiative transitions than $\hbar\omega_{21}$. Indeed, in a typical 4-level dye, the vibrational-rotational structure is very complex and includes many eigenmodes. As a result, the electronic excitation energy will primarily thermalize through available vibronic states directly to the lowest energy level, which is 0.

From the quasi-stationary solution of the rate equations for the population densities N_i in an idealized 4-level system, it follows (see Kristanz,[S13] Sections 2.2.4 and 2.2.1) that

$$N_2 = \frac{N_\mathrm{tot}W_\mathrm{p}}{W_\mathrm{p} + W_\mathrm{s} + \gamma_{21}} \quad \text{and} \quad W_\mathrm{s} + \gamma_{21} = \gamma_{32}\frac{N_3}{N_2} = \gamma_{10}\frac{N_1}{N_2}, \tag{S10}$$

with which we can transform Eq. (S9) to

$$Q_\mathrm{G} = \left(\hbar\omega_{20}\gamma_{20,\mathrm{nr}} + (\hbar\omega_{30}\gamma_{30,\mathrm{nr}}/\gamma_{32} + \hbar\omega_{10} + \hbar\omega_{32})(W_\mathrm{s} + \gamma_{21})\right)\frac{N_\mathrm{tot}W_\mathrm{p}}{W_\mathrm{p} + W_\mathrm{s} + \gamma_{21}}. \tag{S11}$$

Neglecting the non-radiative decay channel $\gamma_{20,\mathrm{nr}} \ll W_\mathrm{s} + \gamma_{21}$ and assuming fast relaxation $\gamma_{32} \gg \gamma_{30,\mathrm{nr}}$ finally yields

$$Q_\mathrm{G} = N_\mathrm{tot}(\hbar\omega_{10} + \hbar\omega_{32})\frac{W_\mathrm{p}(W_\mathrm{s} + \gamma_{21})}{W_\mathrm{p} + W_\mathrm{s} + \gamma_{21}} \tag{S12}$$

for the heat source in the gain material.

The stationary solution for a continuously heated, spherical nanoparticle with Kapitza resistance

In the ambient, the stationary heat equation is

$$\Delta T(\mathbf{r}) = 0 \quad \text{with} \quad r > a, \tag{S13}$$

with the solution

$$T(r > a) = \frac{a}{r} T_2 + T_0, \tag{S14}$$

where T_2 is the stationary surface temperature rise (with respect to the background temperature T_0) on the ambient side and a is the nanoparticle radius. The flux J over the boundary S is continuous and fulfills Eq. (11),

$$J\big|_S = G(T_1 - T_2) = -k_\text{a} \frac{\partial}{\partial r} T(r)\big|_{r=a} = \frac{k_\text{a}}{a} T_2, \tag{S15}$$

where k_a is the thermal conductivity of the ambient and T_1 is the stationary surface temperature rise on the particle side of the interface. Then, the relative change in temperature at the boundary is

$$\frac{T_1 - T_2}{T_2} = \frac{k_\text{a}}{Ga}, \tag{S16}$$

which is inversely proportional to the nanoparticle radius a.

Quasistatic spasing condition for confocal spheroidal core-shell structures

Before solving Maxwell's equations for a spaser numerically, it is often a good idea to look at their quasistatic approximation (i.e., neglecting retardation). It can be used when the

structure under study is much smaller than the typical wavelength. Practically, this means that the wave vector k is neglected in Maxwell's equations. The resulting equations can often be solved analytically and do not contain magnetic fields.

Bohren and Huffman[S14] derived a quasistatic solution for the polarizability α of a confocal spheroidal core-shell structure in an infinite ambient (see Section 5.4, Eq. (5.35)),

$$\alpha = \frac{V\big((\varepsilon_2 - \varepsilon_3)\big(\varepsilon_2 + (\varepsilon_1 - \varepsilon_2)(L_1 - hL_2)\big) + h\varepsilon_2(\varepsilon_1 - \varepsilon_2)\big)}{\big(\varepsilon_2 + (\varepsilon_1 - \varepsilon_2)(L_1 - hL_2)\big)\big(\varepsilon_3 + (\varepsilon_2 - \varepsilon_3)L_2\big) + hL_2\varepsilon_2(\varepsilon_1 - \varepsilon_2)}, \tag{S17}$$

where ε_1, ε_2 and ε_3 are the dielectric functions of core, shell and ambient, V is the total volume of the structure and $h < 1$ is the volume fraction of the core spheroid to the entire structure. The function $L_i = L(e_i)$ depends on (i) the eccentricities e_1 and e_2 of the core and shell spheroids, (ii) the polarization of the incident electric field and (iii) on whether the spheroids are oblate or prolate. Note that the definition of the eccentricity depends on the shape of the spheroid,

$$e = \sqrt{1 - \frac{c^2}{a^2}} \quad \text{with} \quad c < a \quad \text{(oblate)},$$
$$e = \sqrt{1 - \frac{a^2}{c^2}} \quad \text{with} \quad c > a \quad \text{(prolate)}, \tag{S18}$$

where c is the semi-axis parallel to the axis of revolution. If the incident electric field is parallel to the axis of revolution, then

$$L(e) = L_z(e) = e^{-2}\big(1 - e^{-1}\sqrt{1 - e^2}\arcsin(e)\big) \qquad \text{(oblate)},$$
$$L(e) = L_z(e) = (1 - e^{-2})\left(1 - (2e)^{-1}\ln\left(\frac{1+e}{1-e}\right)\right) \qquad \text{(prolate)}. \tag{S19}$$

If the polarization of the incident field is perpendicular to the axis of revolution, then

$$L(e) = L_{x,y}(e) = \frac{1 - L_z(e)}{2}, \tag{S20}$$

S8

where L_z is the appropriate function from Eqs. (S19). By neglecting saturation effects (which is usually justified near the threshold) and tuning the spaser to the $2 \to 1$ transition of the chromophores (meaning $\omega_s = \omega_{21}$), the gain dielectric function (1) simplifies to

$$\varepsilon_G = \varepsilon_h - i\varepsilon_{L,thr} \tag{S21}$$

at the threshold. The spasing threshold corresponds to the polarization going to infinity in the unsaturated case, meaning that the fields in the structure become very high for very small incident fields. In other words, sustained oscillations become mathematically possible as a solution of a homogeneous equation, i. e., without incident field at all. This yields the following condition for the denominator of Eq. (S17),

$$\left(L_1\varepsilon_1 + (1 - L_1)\varepsilon_2\right)\left(L_2\varepsilon_2 + (1 - L_2)\varepsilon_3\right) + hL_2(1 - L_2)(\varepsilon_1 - \varepsilon_2)(\varepsilon_2 - \varepsilon_3) = 0, \tag{S22}$$

which can be solved to estimate the spasing threshold. Since the complex-valued condition (S22) should be fulfilled at the threshold wavelength ω_{thr}, we can numerically look for solution-pairs $(\omega_{thr}, \varepsilon_{L,thr})$. By doing a sweep over several aspect ratios, we can estimate which aspect ratio is favorable in terms of spasing frequency and threshold. For gain-core/metal-shell structures, there exist three solution branches *per polarization of the incident field* that all fulfill condition (S22). They represent different surface plasmon oscillations:[S15] the highest-wavelength solution branch corresponds to the surface charges at the inner and outer surface of the metal shell oscillating *in phase* ("bonding" plasmon), while for the lowest-wavelength branch the charges oscillate *in anti-phase* ("antibonding" plasmon). It can be shown that the middle-wavelength branch always has the highest gain threshold and is thus of no interest for us. When plotted over the aspect ratio, the three solution branches only exist up until some aspect ratio κ_0. At $\kappa = \kappa_0$, two branches merge and vanish simultaneously: for $\kappa > \kappa_0$, only one branch remains (see e. g., Fig. S1b). Thus, finding a single solution point is usually not sufficient for a complete analysis of a spaser.

S9

Table S1: Quasistatic results for eight different core/shell spaser configurations with shell thickness (along all semi-axes) equal to major semi-axis $h = a$. The core aspect ratio is varied from 1 (spherical) to 8 (spheroidal), larger aspect ratios would lead to unrealistically thin structures. The shape of the spasers can be either prolate (cigar-shaped) or oblate (pancake-shaped) spheroidal. The pumping field can either be parallel ($\mathbf{E} \parallel \mathbf{z}$) or perpendicular ($\mathbf{E} \parallel \mathbf{x}$) to the axis of revolution $\mathbf{z}$. In the reference FEM calculations (see Main Text), the values for the shell thickness and major semi-axis are $h = a = 23\,\mathrm{nm}$ for the prolate metal-core/gain-shell and $h = a = 30\,\mathrm{nm}$ for the oblate gain-core/metal-shell spaser. Every gain-core/metal-shell configuration has three solution branches for the quasistatic spasing condition (S22), each corresponding to different surface plasmon oscillations.[S15] The middle-wavelength branch was omitted in the table, since it always has much higher gain threshold.

Core/Shell	Pol.	Shape	Gain threshold	Generation wavelength
Metal/Gain	$\mathbf{E} \parallel \mathbf{z}$	Prolate	$0.02 < \varepsilon_{\mathrm{L,thr}} < 0.12$	$395\,\mathrm{nm} < \lambda_{\mathrm{thr}} < 1177\,\mathrm{nm}$
Metal/Gain	$\mathbf{E} \parallel \mathbf{z}$	Oblate	$0.12 < \varepsilon_{\mathrm{L,thr}} < 1.66$	$329\,\mathrm{nm} < \lambda_{\mathrm{thr}} < 395\,\mathrm{nm}$
Metal/Gain	$\mathbf{E} \parallel \mathbf{x}$	Prolate	$0.12 < \varepsilon_{\mathrm{L,thr}} < 0.25$	$359\,\mathrm{nm} < \lambda_{\mathrm{thr}} < 395\,\mathrm{nm}$
Metal/Gain	$\mathbf{E} \parallel \mathbf{x}$	Oblate	$0.04 < \varepsilon_{\mathrm{L,thr}} < 0.12$	$395\,\mathrm{nm} < \lambda_{\mathrm{thr}} < 697\,\mathrm{nm}$
Gain/Metal	$\mathbf{E} \parallel \mathbf{z}$	Prolate	$0.53 < \varepsilon_{\mathrm{L,thr}} < 34.52$ $0.96 < \varepsilon_{\mathrm{L,thr}} < 14.44$	$412\,\mathrm{nm} < \lambda_{\mathrm{thr}} < 455\,\mathrm{nm}$ $326\,\mathrm{nm} < \lambda_{\mathrm{thr}} < 333\,\mathrm{nm}$
Gain/Metal	$\mathbf{E} \parallel \mathbf{z}$	Oblate	$0.07 < \varepsilon_{\mathrm{L,thr}} < 0.53$ $0.83 < \varepsilon_{\mathrm{L,thr}} < 1.74$	$401\,\mathrm{nm} < \lambda_{\mathrm{thr}} < 537\,\mathrm{nm}$ $333\,\mathrm{nm} < \lambda_{\mathrm{thr}} < 351\,\mathrm{nm}$
Gain/Metal	$\mathbf{E} \parallel \mathbf{x}$	Prolate	$0.52 < \varepsilon_{\mathrm{L,thr}} < 1.11$ $0.39 < \varepsilon_{\mathrm{L,thr}} < 0.96$	$370\,\mathrm{nm} < \lambda_{\mathrm{thr}} < 412\,\mathrm{nm}$ $333\,\mathrm{nm} < \lambda_{\mathrm{thr}} < 353\,\mathrm{nm}$
Gain/Metal	$\mathbf{E} \parallel \mathbf{x}$	Oblate	$0.53 < \varepsilon_{\mathrm{L,thr}} < 6.13$ $0.96 < \varepsilon_{\mathrm{L,thr}} < 4.51$	$412\,\mathrm{nm} < \lambda_{\mathrm{thr}} < 419\,\mathrm{nm}$ $327\,\mathrm{nm} < \lambda_{\mathrm{thr}} < 333\,\mathrm{nm}$

Quasistatic calculations often underestimate the gain threshold for structures of realistic size, where retardation and radiative losses start to play a role comparable with absorption. For a system with a small gain core and a thick metal shell, however, quasistatic predictions can be very accurate.

Table S1 shows the quasistatic results of eight core/shell spaser configurations with equal major semi-axis and shell thickness $a = h$. The aspect ratio is varied from 1-8 to avoid unrealistically thin structures. As long as geometrical similarity $a = h$ is preserved, these results hold for quasistatic structures of arbitrary size. Here, we imply $a = h = 30\,\mathrm{nm}$ for an oblate spaser, and $a = h = 23\,\mathrm{nm}$ for a prolate one. Strictly speaking, Eq. (S22) only holds for confocal (quasistatic) spheroids – however, it still gives a reasonable approximation for
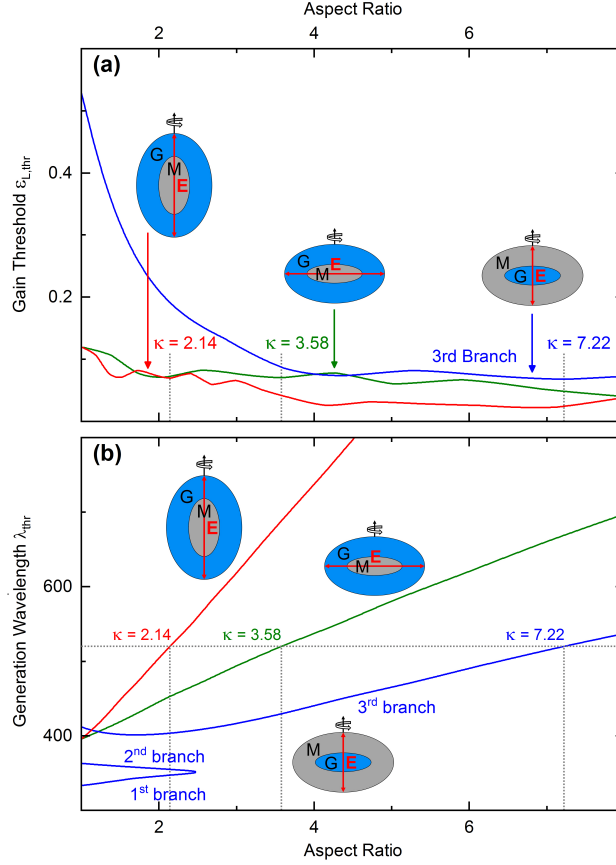
Figure S1: Quasistatic calculations for three spaser configurations: prolate metal-core/gain-shell $\mathbf{E} \parallel \mathbf{z}$ (red), oblate metal-core/gain-shell $\mathbf{E} \parallel \mathbf{x}$ (green) and oblate gain-core/metal-shell $\mathbf{E} \parallel \mathbf{z}$ (blue). **(a)** Gain thresholds and **(b)** generation wavelengths over the range of realistic aspect ratios. The dotted grey lines indicate the aspect ratios with a generation wavelength of 520 nm, where the gain thresholds have local minima. For the gain-core/metal-shell structure, the gain thresholds of the first and second branches are out of range in the plot (see Table S1).

our geometries.

Three spaser configurations have low gain thresholds ($\varepsilon_{\mathrm{L,thr}} < 0.15$) and generation frequencies in the visible range (see Figs. S1a-b). We choose to simulate the oblate gain-core/metal-shell structure with $\mathbf{E} \parallel \mathbf{z}$ and the prolate metal-core/gain-shell structure with $\mathbf{E} \parallel \mathbf{z}$. The spasers are tuned to a generation wavelength of 520 nm: there, the gain threshold has a local minimum and the (quasistatic) aspect ratios are realistic.

Due to appreciable retardation effects, the quasistatic approximation provides a rough es-

Table S2: Exact numeric threshold values and core aspect ratios for the spaser configurations under study.

Spaser configuration	κ	$\varepsilon_{\mathrm{L,thr}}$	λ_{thr}
Oblate gain-core/metal-shell	6.25	0.1133	519.96 nm
Prolate metal-core/gain-shell	1.94	0.1159	519.78 nm

timation of the gain threshold, generation frequency and necessary shape of a core-shell spaser. Using FEM simulations, we can find the exact numeric values, see Table S2. The final geometries are shown in Fig. 2 in the Main Text.

Temperature-dependent Drude model

Since the thermal and electromagnetic problems are coupled via a temperature-dependent dielectric function of the metal component in the spaser, a proper description of the thermal behavior of the latter is necessary. This has been extensively measured for various metals. For example, an overview of the temperature dependence of the dielectric function of gold can be found in Perner[S16] (Section 2.1). For silver, measurements by Sundari et al.[S17] exist, but since their imaginary part is questionably high and their real part changes with temperature, we choose not to use their data. A different approach would be to correct a reliably measured dielectric function using a temperature-dependent Drude model,

$$\varepsilon_{\mathrm{Ag}}(T) = \varepsilon_{\mathrm{Ag}}^{\mathrm{JC}} + \chi_{\mathrm{Ag}}^{\mathrm{Dr}}(T) - \chi_{\mathrm{Ag}}^{\mathrm{Dr}}(T_0), \tag{S23}$$

$$\varepsilon_{\mathrm{Ag}}^{\mathrm{Dr}}(T) = \varepsilon_{\infty} + \chi_{\mathrm{Ag}}^{\mathrm{Dr}}(T), \tag{S24}$$

$$\chi_{\mathrm{Ag}}^{\mathrm{Dr}}(T) = -\frac{\omega_{\mathrm{P}}(T)^2}{\omega(\omega + i\gamma(T))}. \tag{S25}$$

Here, $\varepsilon_{\mathrm{Ag}}^{\mathrm{JC}}$ are the well-known measurements by Johnson and Christy[S18] (measured at room temperature T_0) and $\varepsilon_{\mathrm{Ag}}^{\mathrm{Dr}}$ is a Drude interpolation of the data with temperature-dependent plasma and collision frequency. Do not confuse the Drude plasma frequency ω_{P} with the

pumping frequency of the spaser ω_p.

The temperature-dependence of the plasma frequency is determined by the density and effective mass of free electrons.[S19,S20] Assuming an isotropic material, the density ρ changes due to thermal expansion with

$$\rho(T) = \frac{\rho(T_0)}{\sqrt{1 + 3\alpha(T - T_0)}}, \tag{S26}$$

where α is the linear thermal expansion coefficient. Since α is on the order of $10^{-5}\,\mathrm{K}^{-1}$ for metals, the total change of ω_P over the available temperature range is negligible. According to Reddy et al.,[S20] the change in ω_P due to a temperature-dependent electronic effective mass is less than $10\,\%$ from $300\,\mathrm{K}$ to $900\,\mathrm{K}$. Since both of these effects are small, we omit the temperature-dependence of the plasma frequency for all further purposes.

The thermal behavior of the Drude collision frequency depends on the electron-phonon interaction. According to Ujihara,[S21] the temperature-dependence of electron-phonon scattering can be described via

$$\gamma(T) = \gamma(T_0)\frac{f(T)}{f(T_0)} \quad \text{with} \quad f(T) = T^5 \int_0^{\theta/T} \frac{z^4 dz}{e^z - 1}, \tag{S27}$$

where $\gamma(T_0)$ is the collision frequency at room temperature calculated via Drude interpolation and θ is the Debye temperature. Using the temperature-dependent measurements for the Debye temperature by Simerská[S22] ($\theta(300\,\mathrm{K}) \approx 210\,\mathrm{K}$ and $\theta(1000\,\mathrm{K}) \approx 190\,\mathrm{K}$), the temperature-dependent dielectric function for silver can be calculated. The parameters of the Drude fit are $\hbar\omega_P = 9.169\,\mathrm{eV}$, $\hbar\gamma = 0.021\,\mathrm{eV}$ and $\varepsilon_\infty = 3.58$. The data was fitted with a least-square method in the range 190-1900 nm, which emphasizes longer wavelengths. The results agree with the measurements of the temperature-dependent dielectric function of silver thin films by Reddy et al.[S20]

Because of $\omega \gg \gamma$, Eq. (S23) can be Taylor-expanded as:

$$\varepsilon_{\mathrm{Ag}}(T) - \varepsilon_{\mathrm{Ag}}^{\mathrm{JC}} = i\frac{\omega_{\mathrm{P}}^2}{\omega^3}\left(\gamma(T) - \gamma(T_0)\right) + \mathcal{O}\left(\frac{\gamma^2}{\omega^2}\right). \tag{S28}$$

This shows that the changes in the real part of the dielectric function are negligible. The integrand of f in Eq. (S27) can also be Taylor-expanded at elevated temperatures, which yields for γ:

$$\gamma(T) \approx \gamma(T_0)\frac{5T - 2\theta}{5T_0 - 2\theta}. \tag{S29}$$

Thus, the imaginary part of $\varepsilon_{\mathrm{Ag}}$ increases approximately linearly with temperature.

Quasistatic estimation for the temperature dependence of the spasing field at the threshold generation frequency

In a quasistatic core/shell spaser, the electric field $\mathbf{E}$ in the gain core is almost constant and is given by Eq. (34) in Arnold et al.:[S7]

$$|\mathbf{E}(\omega)|^2 = E_{\mathrm{sat}}^2\left(1 + \left(\frac{\omega - \omega_{\mathrm{thr}}}{\gamma_{\mathrm{L}}/2}\right)^2\right)\left(\frac{\varepsilon_{\mathrm{L}}}{\varepsilon_{\mathrm{L,thr}}} - 1)\right). \tag{S30}$$

Considering it on resonance ($\omega = \omega_{\mathrm{thr}}$) and using the two-material approximation for the spasing threshold (Eq. (11) in Arnold et al.[S12]),

$$\varepsilon_{\mathrm{L,thr}} = \frac{\varepsilon_{\mathrm{M}}''}{|\varepsilon_{\mathrm{M}}'|}\varepsilon_{\mathrm{h}}, \tag{S31}$$

yields

$$|\mathbf{E}(\omega_{\mathrm{thr}})|^2 = E_{\mathrm{sat}}^2\left(\frac{\varepsilon_{\mathrm{L}}|\varepsilon_{\mathrm{M}}'|}{\varepsilon_{\mathrm{h}}\varepsilon_{\mathrm{M}}''} - 1\right). \tag{S32}$$

The spasing field in the metal, $\mathbf{E}_s$, is linearly related via boundary conditions to the (approximately constant) electric field in the core of the structure. Thus, the expected temperature dependence of the metal spasing field $\mathbf{E}_s$ at the threshold generation frequency ω_{thr} is:

$$|\mathbf{E}_s(\omega_{\mathrm{thr}}, T)|^2 \propto E_{\mathrm{sat}}^2 \left(\frac{\varepsilon_{\mathrm{L}} |\varepsilon_{\mathrm{M}}'|}{\varepsilon_{\mathrm{h}} \varepsilon_{\mathrm{M}}''(T)} - 1 \right). \tag{S33}$$

This is Eq. (14) from the main text. Due to approximations used, especially the assumptions of the gain core and the two-materials threshold (S31), it can serve as a guideline only. With three materials, one can find the threshold from the zero of the denominator in (S17) (expression (S22)). This replaces ϵ_{h} by $\epsilon_{\mathrm{h}}+f$, where f is a cumbersome combination of parameters, which, however, does not change the qualitative trends. Numerical results confirm that a similar decrease of metal field with temperature persists also for the prolate metal-core/gain-shell geometry. However, such analytical estimations are less justified there due to variations in saturation across the gain material.

Cooling time

Figure S2 shows the same data as in Fig. 3, but in a linear scale for both axes and on a far longer time scale including a *purely thermal* cooling simulation. The metal-core/gain-shell structure has much shorter cooling times. This is related to the higher temperature gradients leading to a larger heat flux to the ambient; besides, in non-stationary regime, the cooling time for an arbitrary structure is typically similar to its heating time.

Polystyrene as gain host material

In Kristanz,[S13] we also simulated similar spasers with polystyrene (PS) as gain host material. PS was recently used as a matrix for organic dyes in microresonators,[S23–S25] and
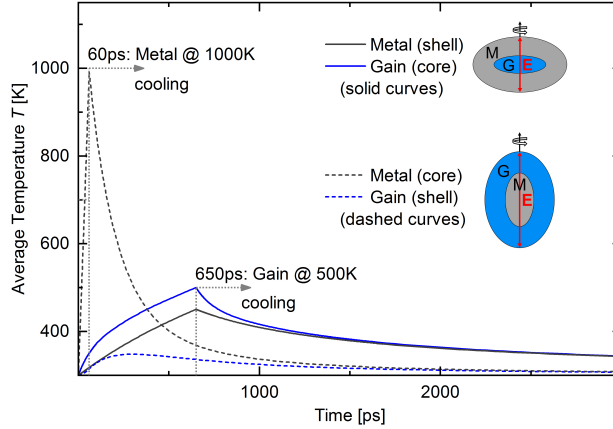
Figure S2: The average temperature T in the respective spaser components (metal and gain). Solid curves are for the oblate gain-core/metal-shell, dashed curves for the prolate metal-core/gain-shell spaser. The maximum operation time is 650 ps and 60 ps, respectively. The dotted grey lines indicate the end of spaser operation and the start of a purely thermal cooling simulation.

was also modeled in other spaser simulations.[S7,S12] The PS-based spasers turn out to be much more heat sensitive than the silica-based ones because of lower thermal stability of PS (melting point is 510-540 K instead of 1986 K for silica[S26,S27]) and its inferior thermophysical properties (thermal conductivity is 0.155 vs. 2.4 W/(m K), thermal diffusivity is 1.2×10^{-3} vs. 8.5×10^{-3} cm^2/s for silica[S27–S32]). As a result, the PS spasers can only operate for 110 ps (oblate gain-core/metal-shell) and 45 ps (prolate metal-core/gain-shell), before the PS melting point is reached. This compares unfavorably with the 650 ps and 60 ps for the silica case.

References

(S1) Stockman, M. I. The spaser as a nanoscale quantum generator and ultrafast amplifier. *Journal of Optics* **2010**, *12*, 024004.

(S2) Khurgin, J. B.; Sun, G. Comparative analysis of spasers, vertical-cavity surface-emitting lasers and surface-plasmon-emitting diodes. *Nature Photonics* **2014**, *8*, 468–473.

(S3) Purcell, E. M.; Torrey, H. C.; Pound, R. V. Resonance Absorption by Nuclear Magnetic Moments in a Solid. *Physical Review* **1946**, *69*, 37–38.

(S4) Yariv, A. *Quantum Electronics*, 3rd ed.; John Wiley & Sons, New York, 1989.

(S5) Kewes, G.; Herrmann, K.; Rodríguez-Oliveros, R.; Kuhlicke, A.; Benson, O.; Busch, K. Limitations of Particle-Based Spasers. *Physical Review Letters* **2017**, *118*, 237402.

(S6) Landau, L. D.; Lifshitz, E. M. *Electrodynamics of Continuous Media*, 2nd ed.; Pergamon Press, Oxford, 1984.

(S7) Arnold, N.; Piglmayer, K.; Kildishev, A. V.; Klar, T. A. Spasers with retardation and gain saturation: electrodynamic description of fields and optical cross-sections. *Optical Materials Express* **2015**, *5*, 2546–2577.

(S8) Saleh, B. E. A.; Teich, M. C. *Fundamentals of Photonics*, 2nd ed.; John Wiley & Sons, Hoboken, 2007.

(S9) Khurgin, J. B. Relative merits of phononics vs. plasmonics: the energy balance approach. *Nanophotonics* **2018**, *7*, 305–316.

(S10) Stockman, M. I. Nanoplasmonics: past, present, and glimpse into future. *Optics Express* **2011**, *19*, 22029–22106.

(S11) Premaratne, M.; Stockman, M. I. Theory and technology of SPASERs. *Advances in Optics and Photonics* **2017**, *9*, 79–128.

(S12) Arnold, N.; Hrelescu, C.; Klar, T. A. Minimal spaser threshold within electrodynamic framework: Shape, size and modes. *Annalen der Physik* **2016**, *528*, 295–306.

(S13) Kristanz, G. V. Thermal limitations of a spaser. M.Sc. thesis, Johannes Kepler University Linz, 2017; Available: `http://epub.jku.at/obvulihs/content/titleinfo/2581924` (accessed July 30, 2018).

(S14) Bohren, C. F.; Huffman, D. R. *Absorption and Scattering of Light by Small Particles*, 1st ed.; John Wiley & Sons, New York, 1983.

(S15) Prodan, E.; Radloff, C.; Halas, N. J.; Nordlander, P. A Hybridization Model for the Plasmon Response of Complex Nanostructures. *Science* **2003**, *302*, 419–422.

(S16) Perner, M. *Optische Untersuchung der Elektronen- und Gitterdynamik in Edelmetall-Nanopartikeln*, 1st ed.; Shaker, Aachen, 1999.

(S17) Sundari, S. T.; Chandra, S.; Tyagi, A. K. Temperature dependent optical properties of silver from spectroscopic ellipsometry and density functional theory calculations. *Journal of Applied Physics* **2013**, *114*, 033515.

(S18) Johnson, P. B.; Christy, R. W. Optical Constants of the Noble Metals. *Physical Review B* **1972**, *6*, 4370–4379.

(S19) Young, C. Y. The Frequency and Temperature Dependence of the Optical Effective Mass of Conduction Electrons in Simple Metals. *Journal of Physics and Chemistry of Solids* **1969**, *30*, 2765–2769.

(S20) Reddy, H.; Guler, E.; Chaudhuri, K.; Dutta, A.; Kildishev, A. V.; Shalaev, V. M.; Boltasseva, A. Temperature-Dependent Optical Properties of Single Crystalline and Polycrystalline Silver Thin Films. *ACS Photonics* **2017**, *4*, 1083–1091.

(S21) Ujihara, K. Reflectivity of Metals at High Temperatures. *Journal of Applied Physics* **1972**, *43*, 2376–2383.

(S22) Simerská, M. The Temperature Dependence of the Debye Temperature θ of Silver by X-ray Diffraction Measurements. *Acta Crystallographica* **1961**, *14*, 1259–1262.

(S23) Wei, C.; Liu, S. Y.; Zou, C. L.; Liu, Y.; Yao, J.; Zhao, Y. S. Controlled Self-Assembly of Organic Composite Microdisks for Efficient Output Coupling of Whispering-Gallery-Mode Lasers. *Journal of the American Chemical Society* **2015**, *137*, 62–65.

(S24) Ta, V. D.; Chen, R.; Sun, H. D. Tuning Whispering Gallery Mode Lasing from Self-Assembled Polymer Droplets. *Scientific Reports* **2013**, *3*, 1362.

(S25) Okada, D.; Nakamura, T.; Braam, D.; Dao, T. D.; Ishii, S.; Nagao, T.; Lorke, A.; Nabeshima, T.; Yamamoto, Y. Color-Tunable Resonant Photoluminescence and Cavity-Mediated Multistep Energy Transfer Cascade. *ACS Nano* **2016**, *10*, 7058–7063.

(S26) Wünsch, J. R. *Polystyrene: Synthesis, Production and Applications*; Technical Report, 2000.

(S27) Haynes, W. M.; Lide, D. R.; Bruno, T. J. *CRC Handbook of Chemistry and Physics*, 97th ed.; CRC Press, Boca Raton, 2017.

(S28) Patnode, W.; Scheiber, W. J. The Density, Thermal Expansion, Vapor Pressure, and Refractive Index of Styrene, and the Density and Thermal Expansion of Polystyrene. *Journal of the American Chemical Society* **1939**, *61*, 3449–3451.

(S29) Karasz, F. E.; Bair, H. E.; O'Reilly, J. M. Thermal Properties of Atactic and Isotactic Polystyrene. *The Journal of Physical Chemistry* **1965**, *69*, 2657–2667.

(S30) Carwile, L. C. K.; Hoge, H. J. *Thermal Conductivity of Polystyrene: Selected Values*; Technical Report, 1966.

(S31) Lord, R. C.; Morrow, J. C. Calculation of the Heat Capacity of α Quartz and Vitreous Silica from Spectroscopic Data. *The Journal of Chemical Physics* **1957**, *26*, 230–232.

(S32) Jund, P.; Jullien, R. Molecular-dynamics calculation of the thermal conductivity of vitreous silica. *Physical Review B* **1999**, *59*, 13707–13711.